Click Here for Full Article

Continuous measurements of discharge from a horizontal acoustic Doppler current profiler in a tidal river

A. J. F. Hoitink,[1,2] F. A. Buschman,[2] and B. Vermeulen[1]

[1]   Acoustic Doppler current profilers (ADCPs) can be mounted horizontally at a river bank, yielding single-depth horizontal array observations of velocity across the river. This paper presents a semideterministic, semistochastic method to obtain continuous measurements of discharge from horizontal ADCP (HADCP) data in a tidal river. In the deterministic part, single-depth velocity data are converted to specific discharge by applying the law of the wall, which requires knowledge of local values of the bed roughness length (z_0). A new filtration technique was developed to infer cross-river profiles of z_0 from moving boat ADCP measurements. Width-averaged values of z_0 were shown to be predominantly constant in time but differed between ebb and flood. In the stochastic part of the method, specific discharge was converted to total discharge on the basis of a model that accounts for the time lag between flow variation in the central part of the river and flow variation near the banks. Model coefficients were derived using moving boat ADCP data. The consistency of mutually independent discharge estimates from HADCP measurements was investigated to validate the method, analyzing river discharge and tidal discharge separately. Inaccuracy of the method is attributed primarily to mechanisms controlling transverse exchange of momentum, which produce temporal variation in the discharge distribution over the cross section. Specifically, development of river dunes may influence the portion of the discharge concentrated within the range of the HADCP.

1. Introduction

[2] Acquiring continuous measurements of river discharge is of paramount importance to water resource management, as it provides the boundary conditions and calibration information required in hydraulic and hydrological models. In small rivers and streams, weirs can be constructed that function as a discharge measurement structure, extending over the entire channel width. Discharge estimation in larger rivers often relies on the validity of rating curves. In general, these are either obtained using moving boat measurements of flow velocity [*Boiten*, 2008], which are labor intensive and difficult to acquire during peak discharges, or using remote sensing information and theory of routing methods [*Perumal et al.*, 2007]. In either of the two approaches, estimates of peak discharges from rating curves are prone to high uncertainty, in particular when floodplains are present. In tidal rivers, the relation between stage and discharge can be considered too complex to attempt to obtain accurate discharges from water levels alone, even when a large data set on flow velocity is available and baroclinic influences on the water motion

are absent. Over the past decade, various techniques have been developed for real-time monitoring of river discharge adopting image-based [*Hauet et al.*, 2008; *Muste et al.*, 2008] or acoustical [*Le Coz et al.*, 2008; *Nihei and Kimizu*, 2008] approaches. In the present study a new method for continuous discharge measurement is presented, which aims to convert velocity data from a horizontally deployed acoustic Doppler current profiler to discharge in a tidal river.

[3] Acoustic Doppler current profilers (ADCPs) are widely used for the analysis of the flow in inland and coastal waters. They were designed to yield vertical profiles of current velocity, pointing either downward from a boat or upward from a rigid frame placed at the river bed. *Chiu and Hsu* [2006] advocated that discharge estimates can be inferred from the maximum velocities at a channel section, which theoretically can be monitored with a single ADCP deployment. In a series of papers [*Chiu and Tung*, 2002; *Chen and Chiu*, 2002, 2004; *Chiu and Hsu*, 2006], Chiu and coworkers have shown that the ratio between mean and maximum velocity remained constant in time for a number of natural and laboratory channels. The location where the maximum flow occurred remained invariable in the natural channels and in the current flume experiments they analyzed. Apart from the dispute about the general validity of a constant horizontal velocity distribution [*Dingman*, 2007], a long-term upward pointing ADCP deployment at a mid-channel location where the maximum velocity occurs is impractical, especially in a navigable river with a mobile

---

[1]Hydrology and Quantitative Water Management Group, Wageningen University, Wageningen, Netherlands.
[2]Institute for Marine and Atmospheric Research Utrecht, Department of Physical Geography, Utrecht University, Utrecht, Netherlands.
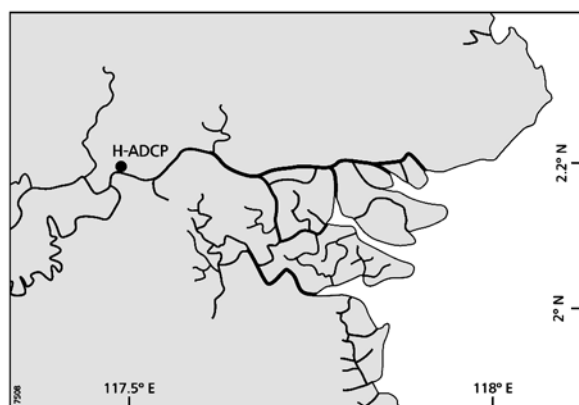
Figure 1. Location map showing the position of the HADCP in the Berau River.

bed. This is the motivation to consider a horizontal deployment of the ADCP, pointing from the shore across a river, toward the center of the channel.

[4] *Marmorino et al.* [1999] were among the first to deploy an ADCP horizontally, to measure near-surface currents in a coastal ocean off one side of an anchored research boat at sea. Using a 307 kHz narrow band ADCP, they obtained consistent current velocity profiles over a distance of 100 m at 0.6 m below the surface. Regarding horizontal ADCP deployments, there are two main potential limitations to consider. First, the beam width increases with distance from the transducer, and the weighing of the returns across the beam width is not entirely uniform. Beam spreading is particularly relevant for a horizontal deployment, as vertical shear is characterized by much smaller spatial scales than horizontal shear. At a distance from the transducer, the horizontal beam may intersect with the water surface or river bed. Secondly, backscatter from sidelobes may overwhelm the backscatter from the main acoustic beam, contaminating the velocity estimates. Physically, it is unlikely that sound waves along sidelobes toward the surface will scatter back to the transducer, because of the small angle between the acoustic path of the main sidelobe toward the water surface and a horizontal plane. In a river deployment, an irregular bed morphology is a potential error source, especially if bed forms are present that may mirror part of the sidelobe energy back toward the transducers. In the present study, errors caused by sidelobes were prevented by choosing a deployment location in the outer bend of a river, at a steep bank.

[5] Apart from instrumental specifications, the measurable range of ADCPs primarily depends on sound attenuation by suspended solids [see, e.g., *Hoitink and Hoekstra*, 2005]. Range limitations and beam spreading imply that it may be infeasible to cover the entire stream width of large rivers. Therefore, theory is needed to convert array data of horizontal velocity components, at a single horizontal profile along part of a river cross section, to total discharge. In shallow rivers, specific discharges within the measurable range of the HADCP can be estimated applying the law of the wall up to the surface, converting single point velocity measurements to depth-mean velocity. In the present approach, partial discharge in the measurement range are subsequently related to total discharge in a stochastic

manner, accounting for a possible time lag between velocity variation near the left bank and near the right bank. Calibration data are obtained from moving boat ADCP measurements.

[6] Approaches to convert HADCP velocity measurements to discharge can be categorized into two classes: deterministic and stochastic. *Nihei and Kimizu* [2008] recently employed a deterministic approach, aiming to assimilate HADCP with a hydrodynamic model. The approaches of *Le Coz et al.* [2008] contain both stochastic and deterministic elements. They describe the index velocity method (IVM), in which the gauged section-averaged velocity is linearly regressed with HADCP data, averaged over a reliable subrange. In the velocity profile method (VPM) they use, the total discharge is computed from theoretical vertical velocity profiles made dimensional with the HADCP velocity measurements across the section, and integrated over the flow depth. In the VPM method, *Le Coz et al.* [2008] extrapolated those depth-averaged velocities using three different approaches: (1) by assuming a constant velocity distribution over the cross section, which was estimated from boat measurements, (2) by assuming a constant Froude number, and (3) by assuming a constant mean velocity throughout the section. Over 18 gauging campaigns, the IVM method was shown to yield most accurate discharge estimates, followed by the VPM method assuming a constant Froude number. The method presented in the present paper combines the IVM and VPM methods, by applying a linear regression between specific discharge, obtained from HADCP data, and total discharge. It extends the theory by allowing for a time lag between variation of specific discharge and total discharge, which is relevant in tidal areas, or in wide inland rivers where discharges feature strong temporal gradients.

[7] The structure of this paper is as follows. Section 2 presents the field data and processing methods, and specifies the river cross section chosen as a discharge measurement station. Section 3 describes the flow structure in the river bend, focusing on the validity domain of the law of the wall and on transverse profiles of longitudinal depth-mean velocity. In section 4 the methodology to determine z_0 is explained and applied. In section 5 total discharges are calculated from HADCP measurements, and compared with corresponding estimates from moving boat ADCP measurements alone. Sections 7 and 8 present a discussion and conclusions.

2. Field Site and Data Acquisition

[8] The study is based on measurements taken in a 400 m wide cross section in the River Berau in East Kalimantan, Indonesia, which has a mean depth around 7 m (Figure 1). A 600 kHz HADCP manufactured by RD Instruments was mounted on a solid wooden jetty in a mildly curved river bend, used as a petrol station. The location in an outer bend was preferred over other possible locations in river reaches with a smaller sinuosity, because of the robustness of the jetty construction, and the pool in the bed morphology in front of the jetty that may avoid the corruption of HADCP data by acoustic side lobe effects. The position on the jetty where the HADCP was mounted was at 0.6 m below the lowest water level during the measurements under consideration. The site is located 25 km upstream of the apex of
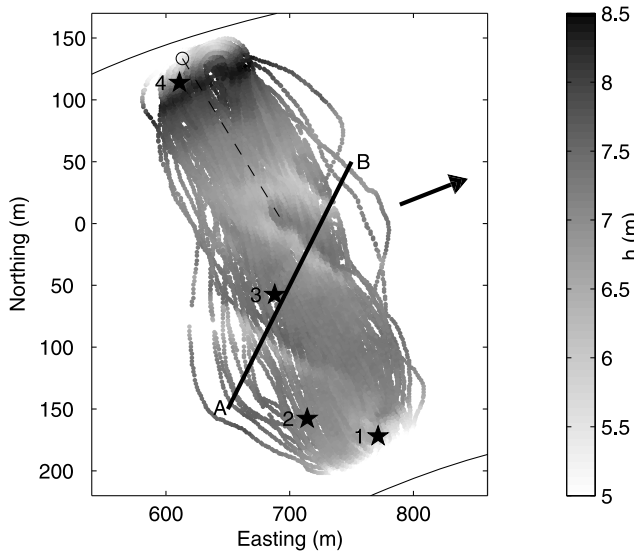
Figure 2. Local bathymetry from ADCP bottom tracking and GPS positioning. Easting and northing coordinates correspond to UTM50E minus 5.55×10^5 m and UTM50N minus 2.41×10^5 m, respectively. Stars indicate where bed samples were taken. The circle shows the location of the HADCP, and the dashed line indicates the 150 m range of the HADCP, measured along the n axis of the chosen coordinate system (see Figure 4). The arrow points in the ebb flow direction. Level depths are measured relative to the mean water level over 2 months of observations.

the Berau estuary, well away from the region of salinity intrusion.

[9] A local depth map was constructed using the range estimation from bottom tracking by the boat-mounted ADCP (Figure 2). The range estimates from the four acoustic beams were corrected for pitch and roll of the boat [*Dinehart and Burau*, 2005]. Computing a simple mean of the obtained beam depths yielded a single depth estimate for each ensemble. The effect of water level variation was removed from the depth estimates. The depth map shows that the transect features a complex of three-dimensional dunes, with heights in the order of 1 m (Figure 3). The pool in the outer bend is about 1 m deeper than the mean depth. Both the outer bank and the inner bank have slopes of 0.14. On the basis of the bed morphology, along-channel (s) and cross-channel (n) coordinates were defined. The easting and northing coordinates of the depth map were rotated system-
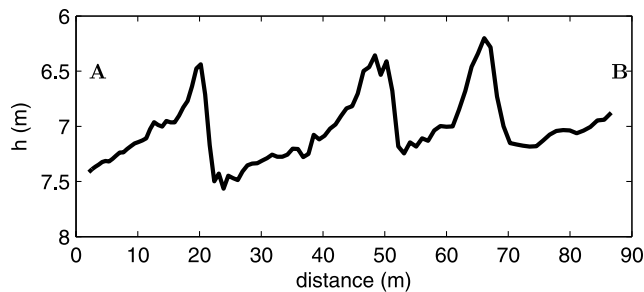

Figure 3. Depth across the transect AB in Figure 2, showing dune profiles.
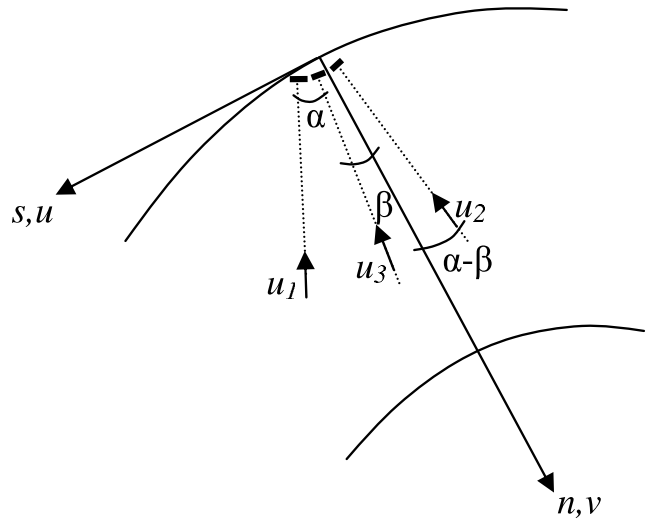

Figure 4. Definition sketch (top view), where u is velocity in the flood direction, coinciding with the s axis; v is velocity toward the inner bend along the n axis, across channel; α is the ADCP beam separation angle; β is the angular difference between the n axis and the axis of the central acoustic beam of the HADCP, measured positive as indicated; and u_1, u_2, and u_3 are the radial velocities along the three acoustic HADCP beams.

atically in steps of 0.5 degrees. For each rotation step, the root-mean-square deviations from mean values in the potential s direction were averaged. Depth variation along the s coordinate was found to be minimal when it deviated $239°$ from the north. On the basis of this analysis, the positive s and n coordinates are defined as $239°$ and $149°$ from the north, respectively. The origin of the adopted coordinate system is at the shoreline (Figure 4). The vertical coordinate, z, points upward and has its origin at the mean water level (Figure 5), which was taken as a reference water level during the 2 months of HADCP measurements. The variation around the mean water level is denoted by η (Figure 5). The tidal range in the Berau River varies from about 1 m at neap tide to about 2.5 m at spring tide. The horizontal velocity components u and v are in the s and n
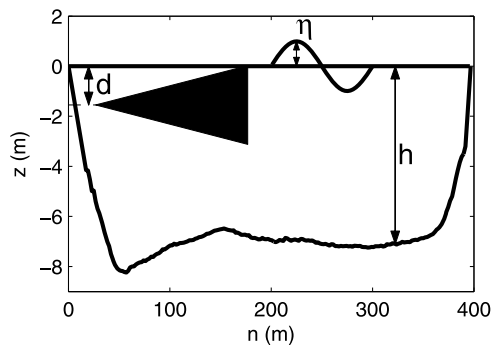

Figure 5. Definition sketch (side view). The cross-river depth profile is obtained by averaging depth estimates from Figure 2 in the s direction. The black shaded area indicates a cross section of the conical measurement volume of the central main lobe of the HADCP.
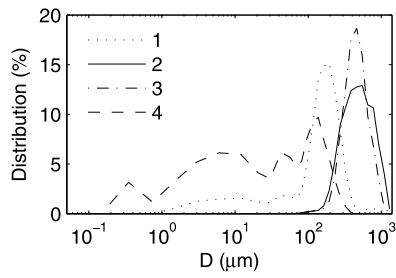
Figure 6. Grain size distribution of bed samples taken at the four locations indicated in Figure 2.

directions, respectively, where positive values of u coincide with upstream flow, or flood (Figure 4).

[10] Four bed samples were taken along the transect, at locations indicated in Figure 2. Figure 6 shows the grain size distributions of those bed samples. The grain size distributions taken in the dune field are unimodal, with an average median grain size diameter (D_{50}) of 457 μm and an average D_{90} of 798 μm, being the grain size at which 10% is coarser. Those values correspond to medium sand. The grain size distributions of the samples taken near the shores are multimodal, and indicate the presence of fine sands, silt and clay.

[11] Two measurement protocols were applied for the HADCP measurements presented herein. A slow-pinging protocol was setup for the period between 6 October 2006 and 20 November 2006, when 1 minute ensembles were stored featuring 15 pings per ensemble and a horizontal cell size of 1 m. For calibration purposes, a fast-pinging protocol was applied within the period between 24 and 26 November 2006, when the HADCP stored single ping ensembles at 1.14 Hz, retaining the 1 m cell size. For both setups, the range to the first cell center was 1.96 m. During the calibration period, moving boat measurements were taken along a cross-channel transect, with a 1.2 MHz RDI broadband ADCP setup in measuring mode 1 and a conventional GPS having an estimated accuracy within 10 m. Those measurements yielded 175 repeated transect observations within a single tidal cycle. Figure 7 shows the variation of η and discharge, denoted by Q, during the calibration period. The transect measurements were regularly distributed over an 11.4 h period. For the boat-mounted ADCP measurements four-ping ensembles were stored at 0.69 Hz, and the depth cell size was set at 0.5 m. When choosing a navigation speed, a trade-off has to be made between error induced by pitch and roll of the boat, and temporal resolution of the measurements. A higher temporal resolution allows to better remove the influence of turbulence in the measurements. A relatively high boat speed of typically 2 m s^{-1} was chosen along the central parts of the transects, where the water velocity ranged between plus and minus 1 m s^{-1}. Near the banks, the boat reduced speed but did not stop. The ensembles rarely spanned over more than 3 m. The range to the first depth cell center was 1.27 m.

[12] The HADCP measures along three beams in a horizontal plane, with $\alpha = 25°$ angles between the beams (see Figure 4). In the current deployment, the pitch of the HADCP was zero degrees and the central beam axis was

rotated by an angle $\beta = 16.3°$ relative to n, in clockwise direction. The along-beam velocities, denoted by u_1, u_2 and u_3, are positive toward the transducers and relate to the $\hat{u}$ and $\hat{v}$ velocity components according to

$$u_1 = -\hat{v}\cos(\alpha + \beta) - \hat{u}\sin(\alpha + \beta) \tag{1}$$

$$u_2 = -\hat{v}\cos(\beta - \alpha) - \hat{u}\sin(\beta - \alpha) \tag{2}$$

$$u_3 = -\hat{v}\cos(\beta) - \hat{u}\sin(\beta) \tag{3}$$

where the ^ symbol is used to indicate that the velocity components can be considered a volume average over an acoustic target cell. Two of the three equations (1)–(3) suffice to calculate $\hat{u}$ and $\hat{v}$. The redundant beam is included in the instrument for error estimation, at the cost of a doubled beam separation. Because the n axis falls between the centerlines of beams 2 and 3, we chose to calculate $\hat{u}$ and $\hat{v}$ from equations (2) and (3), limiting the maximum beam separation to 66.5 m at $n - x = 150$ m. Herein, x is the distance of the transducer from the shoreline, which was 27 m. For the 600 kHz HADCP used in this study, the acoustic beam width ϕ is 1.2 degrees. Figure 5 illustrates a cross section of the conical volume of the central main lobe of the acoustic power, which is centered at a distance $d = 1.55$ m below the mean water level. This shows that the target volume is in the upper part of the water column, where velocity varies almost linearly with depth [*Henderson*, 1966]. A volume-averaged velocity measurement collected by the HADCP at some range from the transducer is therefore assumed to correspond to the centroid of the measurement volume, which is at elevation z_c. Over the range where the acoustic main lobes are submerged, the discrete, 1-m-long measuring volumes can approximated to be cylindrical, with a radius r according to
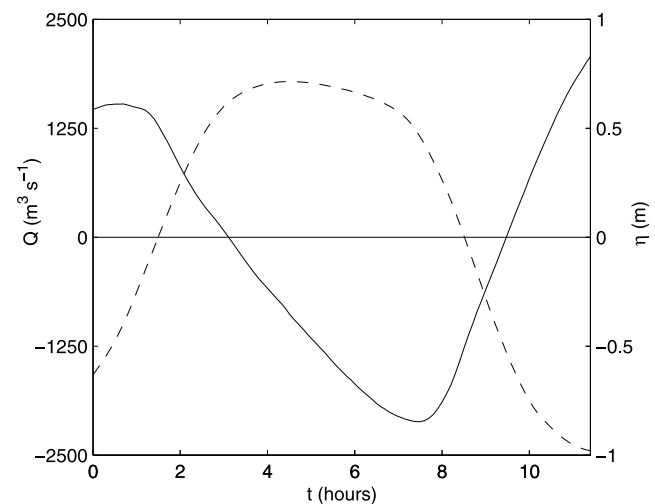
$$r = \tan(\phi/2)(n - x) \tag{4}$$

Figure 7. Variation of η (solid line) and Q (dashed line) during the calibration period.
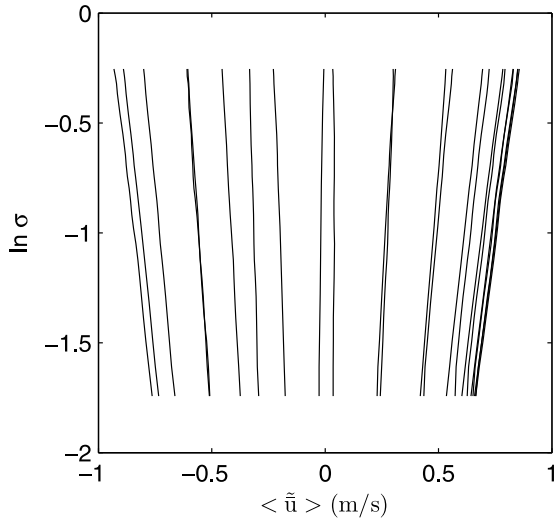
Figure 8. Width-averaged velocity profiles over a tidal cycle, showing that $\langle \bar{\bar{u}} \rangle$ increases linearly with $\ln\sigma$. The law of the wall applies over the full measurement range, even around slack water.

The elevation of the centroid of the submerged part of a discrete measuring volume is calculated from

$$z_c = \begin{cases} -d & \text{if } d + \eta > \tan(\phi/2)(n - x) \\ -d - \Delta z & \text{otherwise} \end{cases} \quad (5)$$

where Δz accounts for the lowering of the centroid of the ensonified water volume if the main lobe intersects with the water surface at low water, which can be calculated from (see Appendix A)

$$\Delta z = \frac{\frac{2}{3}\left(r^2 - (d + \eta)^2\right)^{1.5}}{r^2 \sin^{-1}\dfrac{d + \eta}{r} + (d + \eta)\sqrt{r^2 - (d + \eta)^2} + \frac{1}{2}\pi r^2} \quad (6)$$

At the lowest water level during the measurements, the main lobes intersected with water surface at n = 84 m.

3. Mean Flow Structure and Discharge Distribution

[13] The Doppler-derived velocity obtained from ADCP measurements is composed of four components:

$$\tilde{u} = \bar{u} + u' + N_u + \epsilon_u \quad (7)$$

where a tilde denotes an estimated quantity, an overbar denotes a mean flow component, u' is the contribution by turbulence, N_u is Doppler noise and ϵ_u is error introduced by accuracy limitations regarding the estimation of pitch, roll, heading, and GPS location. A similar expression holds for v. It is assumed that systematic errors related to firmware of the HADCP and inaccuracy of the tilt sensors are negligible, so that the sum of u', N_u and ϵ_u reduces to zero when averaged over a long enough time period. To isolate the mean flow component $\bar{u}$ from the moving boat ADCP

measurements, the following procedure is adopted. The vertical coordinates of the velocity data are transformed to relative height above the bottom, σ, which is defined by

$$\sigma = \frac{z + h}{h + \eta} \quad (8)$$

where h is mean water depth. The moving boat velocity data is stored in bins using a triangle-based, linear interpolation. Those bins coincide with the meshes of an equidistant grid defined along the transect, with a mesh size of 5 m in the n direction, and 0.05 in the σ direction. For each mesh, a time series of $\tilde{u}$ is then obtained. Assuming the mass flux through the meshes of the n-σ grid to be constant in the streamwise direction within the measurement range, the product of $\tilde{u}$ and $(h + \eta)$ is independent of s. Time series of the latter product were subjected to a linear low-pass filter according to the method of *Schlax and Chelton* [1992]. The turnover period of the filter is set at 1.5 h, which is supposed to cover several times the largest turbulence fluctuations, and to be smaller than the smallest time scale of tidal oscillations. The filtered values were divided by $h + \eta$ and averaged in the s direction over the range that was covered during the measurements. The mean velocity estimates obtained accordingly are denoted by $\bar{\bar{u}}(n, \sigma)$.

[14] In a fully developed and fully rough turbulent boundary layer the velocity profile is described by the law of the wall:

$$\frac{\bar{u}(z)}{u_*} = \frac{1}{\kappa} \ln\left(\frac{z + h}{z_0}\right) \quad (9)$$

where κ is the Von Karman constant, z_0 is bottom roughness length and u_* is the shear velocity, which relates to the bottom shear stress τ_b and density ρ as in $u_* = \sqrt{\tau_b/\rho}$. It can be shown that for a water column that satisfies equation (9) up to the surface:

$$\bar{u}(\sigma) = \frac{u_*}{\kappa}(\ln \sigma + 1) + U \quad (10)$$

where U is depth-mean velocity. To investigate the range from the bed to which the vertical profiles of $\bar{\bar{u}}$ satisfy equation (9), Figure 8 displays $\langle \bar{\bar{u}} \rangle$ versus $\ln \sigma$, where the angular brackets denote width averaging. It was chosen to present width-averaged velocity profiles instead of individual profiles of $\bar{\bar{u}}$, because the latter are insufficiently smooth to perceive subtle deviations from a logarithmic profile. Moreover, if an upper portion of the water column is influenced by wind shear or density stratification, this would be manifest throughout the entire transect, and hence also in Figure 8. Figure 8 confirms that in the measurement range of the ADCP, profiles of longitudinal mean flow can be considered logarithmic, even around slack water, when flow profiles are generally least stable.

[15] Values of U were calculated from the intercept of a linear regression line through data points of $\bar{\bar{u}}$ versus $\{\ln(\sigma) + 1\}$ (equation (10)). Figure 9 shows cross-transect profiles of U during the observations. The transect can be subdivided in three regions. In the central part, some 20 m from the inner bank and 100 m from the outer bank, the profile remains nearly uniform over the tidal cycle. Zooming into this region during flood, two peaks can be observed,
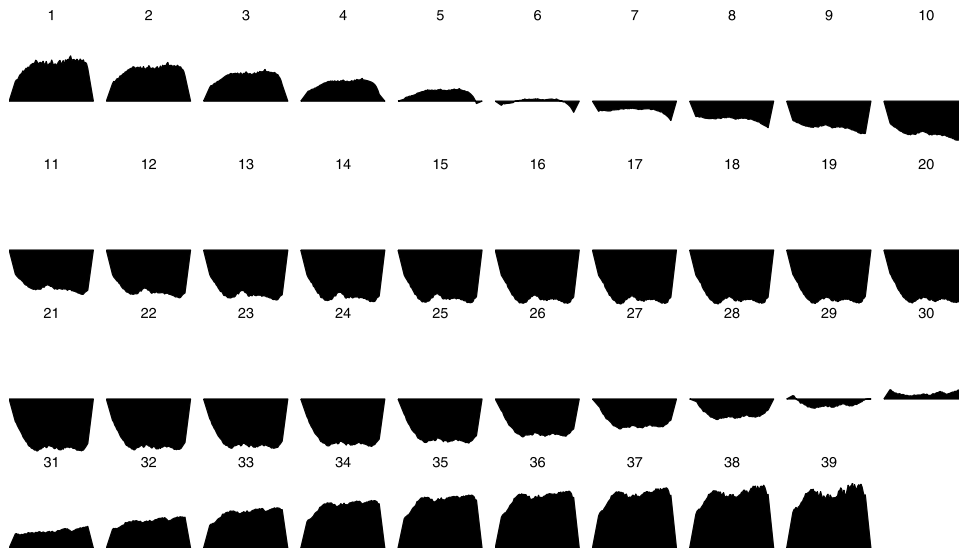
Figure 9. Successive cross-river profiles of U, with the left and right sides of the subplots corresponding to the outer bank and the inner bank, respectively. The interval between the profiles is 18 min.

with the peak near the inner bank being slightly larger than the other. During ebb, a triple peaked profile develops, again with subtle differences in magnitude between the peaks. In the outer bend region, the profile gradually reduces to zero over a distance of about 100 m, in contrast to the inner bend region, where the flow reduces to zero over a distance of about 20 m. It is remarkable that the trench in the outer bend conveys a relatively small portion of the flow. It suggests that the flow conditions observed during the measurements were well below conditions that are formative for the channels in the River Berau. Variation of U in the near uniform central region lags behind variation of U in both the inner bend and the outer bend regions, which can be explained as an effect of inertia.

[16] Peaks in the profiles of U can be partly understood from general knowledge about the physics of steady state longitudinal flow in mildly curved river bends [e.g., *Ikeda et al.*, 1990]. In channels of uniform width, uniform depth and uniform bed roughness, two counteracting mechanisms specify the profiles of U. The imbalance between lateral forces caused by centrifugal acceleration and pressure gradients generate a secondary current, which produces advective transport of longitudinal momentum toward the outer bend. This may cause the humps in profiles of U near the outer bend region, where longitudinal momentum concentrates. The opposite effect can be expected from the increase of the longitudinal slope of the free surface toward the inner bank, where the radius of curvature is smallest. Peaks of U near the inner bank can therefore be explained by greater slopes. The occurrence of a third velocity peak during ebb can be the combined effect of bed forms, depth variation and the complex secondary circulations introduced by width variation.

[17] With the obtained profiles of U, the specific discharge q can be calculated according to

$$q = (h + \eta)U \qquad (11)$$

After linearly extrapolating profiles of q to zero at the shores, where q is set to zero, the total discharge Q can be

obtained by integrating q over width. Aiming to predict Q from q at any place in the cross section, the following linear model is proposed:

$$Q(t) = f(n)Wq(n, t + \tau(n)) \qquad (12)$$

where W is the river width, $f(n)$ is a constant amplification factor and $\tau(n)$ is a time lag function. The independence of $f(n)$ from time will be discussed in section 6. To determine $\tau(n)$, Figure 10 (top) shows the time difference between the occurrence of $q = 0$ and $Q = 0$, both for high water slack and
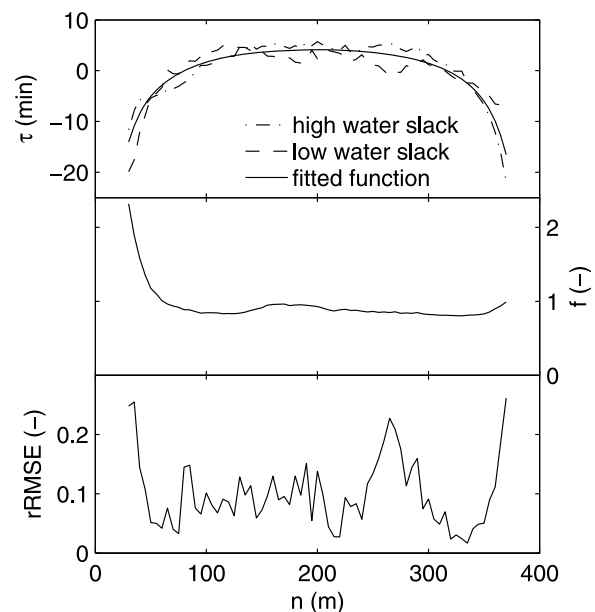

Figure 10. (top) Time difference between the occurrence of $q = 0$ and $Q = 0$ for high-water slack, low-water slack, and a fitted function. (middle) Amplification factor f in equation (12). (bottom) Relative root-mean-square error in modeled values of $Q(t)$.
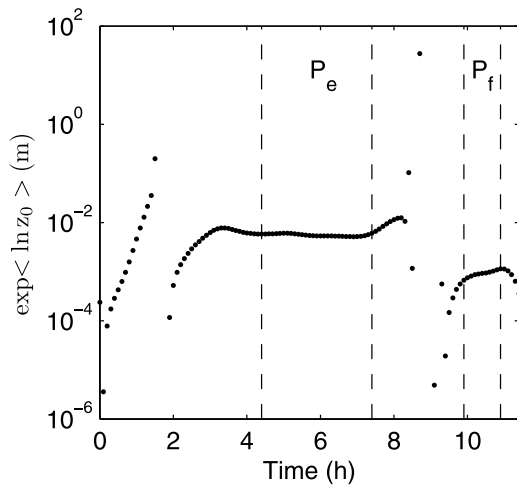
Figure 11. Development of the exponent of the width-averaged natural logarithm of z_0 in time. Within the periods P_e and P_f, which are void of the influence of low-pass filtering, z_0 is approximately constant.

low water slack. The function $\tau(n)$ is supposed to be constant in time, and is approximated by fitting a symmetric function of the form

$$\tau = c_1 \sin(n\pi/(W))^{c_2} + c_3 \qquad (13)$$

to the data from both high-water slack and low-water slack. Herein, c_1, c_2 and c_3 are coefficients with fitted values of -6.8, -0.89 and 10.8, respectively. Figure 10 (middle) displays $f(n)$, obtained by regressing $Q(t)$ and the product of W and $q(n, t + \tau(n))$. It highlights the relatively small discharges in the outer bend region of the transect. Figure 10 (bottom) shows the relative root-mean-square error (rRMSE) of the modeled values of $Q(t)$, where the model refers to equation (12) and the empirical functions $\tau(n)$ and $f(n)$. Values of rRMSE are highest in the regions within 60 m from the river banks and around $n = 265$, within the dune field. For the larger part of the transect, rRMSE remains below 0.15.

4. Bed Roughness Length Estimation

[18] On the basis of dimensional analysis of a rough turbulent boundary layer, and estimation of an integration constant from empirical research, it can be shown that a characteristic length scale of protrusions on the bed (k_b) is a factor 30 larger then z_0 [*Pope*, 2000]. Values of k_b, and therewith z_0, parameterize the length scales involved in skin friction drag induced by the grains at the water-sediment interface and in hydrodynamic form drag caused by bed forms. It also incorporates the influence of sediment movement on hydraulic drag [*Xu and Wright*, 1995]. For a given bottom topography, z_0 is generally considered to be only dependent on the orientation of the flow, and hence independent of velocity magnitude [e.g., *Cheng et al.*, 1999]. For flow in a tidal river, this assumption implies that z_0 at a site can take two values, one pertaining ebb and one pertaining to flood. Direct estimation of z_0 from ADCP velocity profiles is complicated by the lack of near-bed

measurements, where velocity gradients are largest [see also *Biron et al.*, 1998]. To circumvent this problem *Sime et al.* [2007] estimate z_0 from grain sizes. They find support for their estimates by showing that two alternative methods for calculating bed shear stress, which have a different sensitivity to error in the z_0 estimate, yield consistent results. The methodology of *Sime et al.* [2007] cannot take into account the variation of z_0 with orientation of the flow.

[19] Aiming to account for differences in z_0 between ebb and flood, the approach adopted herein persists in inferring z_0 from mean velocity data only, by integrating a large number of normalized velocity profiles. The slopes of the linear regression lines through data points of $\tilde{u}$ versus $\{\ln(\sigma) + 1\}$ coincide with u_*/κ. Values of z_0 can be obtained from the shear velocity according to

$$z_0 = \frac{h + \eta}{\exp\left(\dfrac{\kappa U}{u_*} + 1\right)} \qquad (14)$$

On the basis of a comparison between various methods of calculating roughness lengths, *Cheng et al.* [1999] showed that log averaging of z_0 yields more consistent results than taking the arithmetic mean. Following *Cheng et al.* [1999], Figure 11 shows $\tilde{z}_0$ log averaged over width. During the tidal cycle under study, the end of a flood period, a complete ebb period and the first 3 h of a flood period were monitored consecutively. The systematic variations of the log-averaged values of z_0 during slack water are considered to be artifacts of the low-pass filtering of the data. With the turnover period set at 1.5 h, $\bar{u}$ at slack water is estimated from 45 min of velocity data during flood and 45 min during ebb, covering two periods when the velocity profiles are inherently different. The estimates 45 min from the beginning and 45 min from the end of the measurements were also discarded, because of the asymmetrical low-pass filtering in those time domains. This leaves two continuous periods in which log-averaged z_0 values are valid, one during flood (P_f) and one during ebb (P_e). It can be observed in Figure 11 that, within P_f and P_e, $\exp \langle \ln \tilde{z}_0 \rangle$ is indeed approximately constant. The mean value of $\exp \langle \ln \tilde{z}_0 \rangle$ during P_f is almost a decade smaller than the mean value during P_e.

[20] To obtain local bed roughness lengths during P_f, denoted by z_{0f}, equations (9) and (10) can be elaborated and integrated over P_f, to yield:

$$g(\sigma) = (\ln z_{0f} + 1) F(\sigma) \qquad (15)$$

where:

$$g(\sigma) = \int_{P_f} \left[\frac{\bar{u}(\sigma,t) - U(t)}{U(t)} \ln(h + \eta(t)) - \ln(\sigma) - 1 \right] dt \qquad (16)$$

$$F(\sigma) = \int_{P_f} \left[\frac{\bar{u}(\sigma,t) - U(t)}{U(t)} \right] dt \qquad (17)$$

Values of z_{0f} can then be obtained from the linear regression line, with zero intercept, through calculated values of $g(\sigma)$
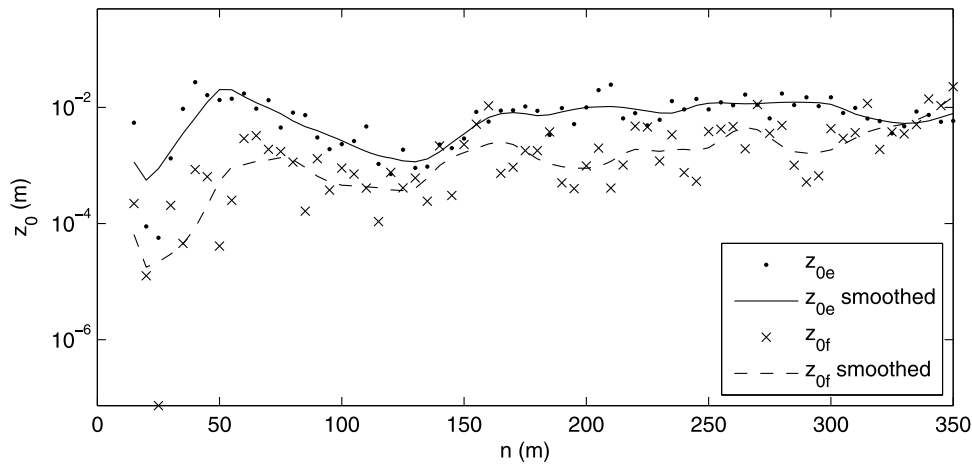
Figure 12. Cross-river profiles of z_{0e} and z_{0f}.

versus $f(\sigma)$. An analogous procedure is followed to calculate z_{0e}. Figure 12 shows cross-river profiles of z_{0e} and z_{0f}, including smoothed lines to remove spatial variations at length scales smaller than 40 m. The relatively large variation in the original estimates of z_{0f} might be attributed to the shorter integration period P_f. Focusing on z_{0e}, the consistency between neighboring estimates is strikingly high. It suggests that contrary to general expectations, values of z_0 can be obtained from moving boat ADCP measurements alone. The smoothed profiles of z_{0f} and z_{0e} covary across the transect, with the roughness lengths values during flood being a decade smaller than during ebb, which was already established from the analysis of width-averaged roughness length values.

[21] Values of both z_{0e} and z_{0f} are smaller in the trench near the bank of the outer bend (see also Figure 5). The reduction of the roughness length can be explained by the fact that the trench conveys a small amount of discharge. The trench will be a region of divergence rather than convergence, and the deepest part of the trench can be relatively inactive. The stagnant layer may then be a smooth boundary of the flow above it. A smaller dip in the profiles of z_{0e} and z_{0f} can be found at the shoal around $n = 130$, where fine sediment may have accumulated. In the region where the oblique dunes occur, the roughness values are approximately constant.

[22] Figure 12 shows that except for a small region near the inner bank, the roughness across the river is systematically lower during P_f. The relatively steady values of z_{0f} and z_{0e} during P_f and P_e, respectively, exclude the possibility that acceleration/deceleration effects play a major role [see also *Soulsby and Dyer*, 1981]. The cause of the lower roughness during flood may relate to the obliquely oriented sand dunes, which are formed by the ebbing flow according to their morphology. Both during ebb and flood the flow near the bed has a component toward the outer bend, due to flow curvature. The angle of approach of the near-bed flow relative to the sand dunes is therefore different between ebb and flood. Bed roughness in a turbulent boundary layer parameterizes local turbulence intensity, which strongly depends on wakes that form in the lee of the sand dunes. In the wakes of the dunes vortices may be created that

develop differently during ebb and flood. The lower roughness during flood can be explained from less intense wake formation. Ebb-dominated bed load sediment transport may also impact the effective drag exerted on the flow, which is reflected in the roughness length.

5. Method to Estimate Discharge From HADCP Data

[23] On the basis of the analysis in the foregoing, a semideterministic, semistochastic model is built to convert HADCP data to discharge. The following procedure is followed. The mean flow component is extracted from the HADCP data by low-pass filtering [*Schlax and Chelton*, 1992], resulting in estimates of $\bar{\bar{u}}$. Time series of $\bar{\bar{u}}$ can be converted to U using equations (8)–(10), which can be elaborated to yield the following expression in U:

$$U = F\hat{u} \tag{18}$$

where the response coefficient F is obtained from:

$$F = \frac{\ln(h + \eta)/(ez_0)}{\ln \sigma_c(h + \eta)/z_0} \tag{19}$$

$$\sigma_c = \frac{h + z_c}{h + \eta} \tag{20}$$

where z_c is calculated from equations (5) and (6). It is assumed that cross-river profiles of both z_{0f} and z_{0e} remain constant during the succession of tidal cycles under study, and therefore equal the smoothed lines displayed in Figure 12. The estimated discharge $\tilde{Q}$ is obtained from $\tilde{U}$ at any location in the measurement range from the HADCP by applying equations (11)–(13), and the values of the coefficients c_1, c_2 and c_3 from section 3.

[24] Figure 13 investigates the sensitivity of the response coefficient F to changes in bed roughness, showing how this coefficient changes with distance from the shore. For low values of z_0, in the range between 10^{-5} m and 10^{-3} m, F changes less than 0.02 when z_0 increases or decreases with a
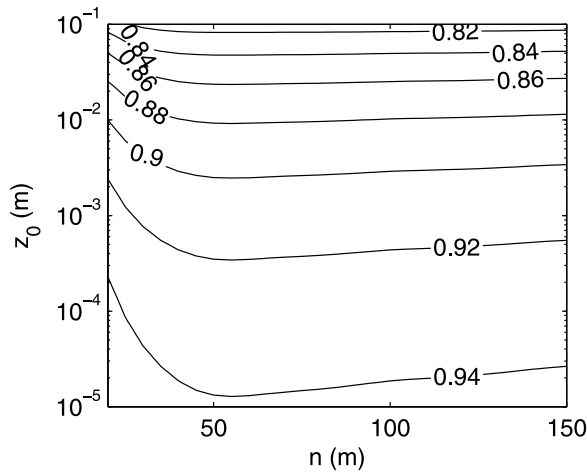
Figure 13. Response coefficient F as a function of z_0 and distances from the shore n.

Figure 15. Scatterplot of U_{bm} versus the relative difference $(U_{sl} - U_{bm})/U_{bm}$ in the midfield range of the HADCP, indicating the relative difference between U_{sl} and U_{bm} as a function of flow strength. In the gray area relative differences are outside the range between -1 and 1.

decade. The sensitivity increases with increasing bed roughness. When z_0 increases with a decade from 10^{-2} m and 10^{-1} m, values of F decrease around 0.07. Those statements hold over the largest part of the measuring domain. Only close to the shore, where depths are smaller, the isolines of F in Figure 13 become denser, indicating a slightly higher sensitivity. Figure 13 illustrates that HADCP estimates of discharge are expected to be more accurate when the river bed is smoother and depths are larger.

[25] The performance of the HADCP can be investigated by comparing U_{bm} and U_{sl}, which denote the depth-mean velocity estimates from boat-mounted ADCP velocity data and from the HADCP, respectively. The root-mean-square deviation ($RMSD$) between U_{bm} and U_{sl} is calculated according to:

$$RMSD = \sqrt{\frac{1}{P_m} \int_{P_m} (U_{sl} - U_{bm})^2 dt} \qquad (21)$$

where P_m is the period of the tidal cycle covered by the boat-mounted data. Figure 14 shows values of $RMSD$ and
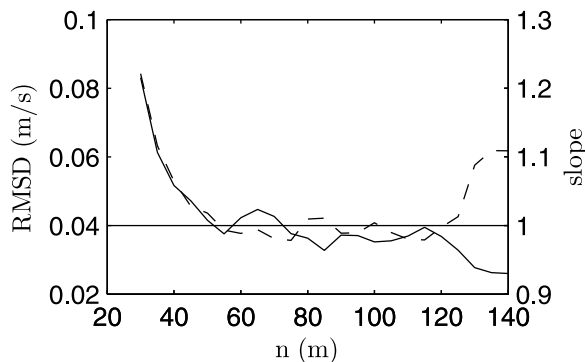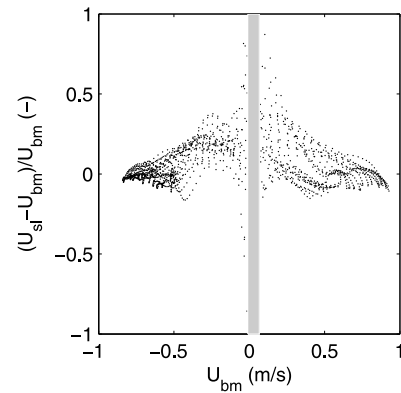

Figure 14. Correspondence between HADCP and boat-mounted ADCP velocity estimates, as a function of distance to the shore, based on RMSD (dashed line) and slopes of regression lines through scatterplots of U_{sl} and U_{bm} (solid line). The horizontal line reflects a slope of 1. The y intercepts of the regression lines vary between -0.03 and 0.02 m s^{-1}.

the slopes of the regression lines through scatterplots of U_{sl} versus U_{bm}, both as a function of n. Three regions can be distinguished. In the near field, $RMSD$ gradually decreases from 0.08 m s^{-1} at $n = 30$ m to 0.04 m s^{-1} at $n = 50$ m, whereas within that range the slopes decrease from 1.2 to 1.0. In the midfield between $n = 50$ m and $n = 120$ m, $RMSD$ takes a steady value of 0.04 and the slopes fluctuate between 0.96 and 1.04. In the far field, slopes of the regression lines gradually decrease to 0.93 at $n = 140$, where $RMSD$ exceeds 0.06 m s^{-1}. Focusing on the midfield range that shows the highest correspondence, Figure 15 shows a scatterplot of U_{bm} versus $(U_{sl} - U_{bm})/U_{bm}$ for all measurements within that range. From Figure 15 it can be concluded there is no unacceptable bias for low or high flow rates. In the near-field region, where the boat turns, the observed differences can be attributed to differences in sampling geometries and inaccuracies in U_{bm} introduced by heave, pitch and roll of the boat. Error introduced by boat movements may explain a weak dependence of the deviation of U_{sl} from U_{bm} on the tidal stage, as the pitch and roll depend on the orientation of the boat relative to the direction of the surface flow. The rigidly mounted HADCP suffers only occasionally from movements caused by boats mooring to the jetty. It can be argued that the error in U_{bm} may have a stronger contribution to $RMSD$ than the error in U_{sl}. In the far-field range, HADCP data can be corrupted by side lobes either from the surface or from the bed.

6. Internal Consistency

[26] Using the method described in section 5, a continuous, six week period of HADCP array velocity data was converted to discharge. Each element in the obtained array contained a time series of $\hat{Q}$, which was independent of the other elements. Improved values of $\hat{Q}$ could be obtained by averaging all the corresponding estimates from the different array elements, but by doing so, information about the internal consistency would be lost. By comparing those mutually independent discharge estimates, an indication could be obtained about the independence of the amplification factor f from time. Therefore, the midfield range is split in two parts, each covering a cross-river reach of 35 m:
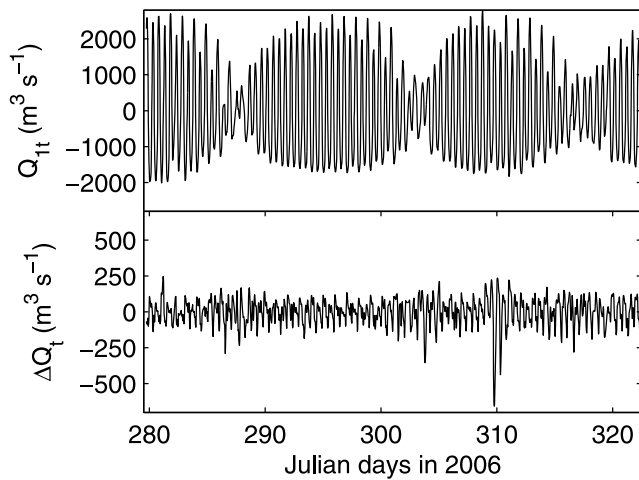
Figure 16. (top) Variation of discharge at tidal frequencies over three successive spring neap cycles from Q_{1t}. (bottom) Variation of ΔQ_t as an indicator of the internal consistency of HADCP measurements at tidal frequencies.

a part near the shore and a part closer to the channel center. The average values of $\hat{Q}$ over the two parts are denoted by $\hat{Q}_1$ and $\hat{Q}_2$, where $\hat{Q}_1$ pertains to the part closest to the shore. By applying a low-pass filter, time series of $\hat{Q}_1$ and $\hat{Q}_2$ were decomposed in a tidal component and a subtidal component. The subtidal component theoretically includes a contribution of river discharge and a contribution of subharmonics, caused by nonlinear tidal interactions [see also *Le Blond*, 1979]. The latter contribution to subtidal discharge generally features a fortnightly variation, which was not observed in our data. Therefore the subtidal component is here referred to as the river discharge. The tidal component and the river component are denoted by the subscripts t and r, respectively.

[27] Figure 16 shows $\hat{Q}_{1t}$ and the difference between $\hat{Q}_{1t}$ and $\hat{Q}_{2t}$, denoted by ΔQ_t, over the six weeks period. The tidal discharges range between 2500 m^3 s^{-1} during flood and -2000 m^3 s^{-1} during ebb. The variance of ΔQ_t does not covary with $\hat{Q}_{1t}$, as the magnitudes of ΔQ_t are similar during spring tides and neap tides. Values of ΔQ_t do vary at tidal frequencies, and average out to -0.1 m^3 s^{-1} over the measuring period. The standard deviation of ΔQ_t is 93 m^3 s^{-1}, and the absolute values remain below 200 m^3 s^{-1} for 97% of the measurement period. A marked extreme occurs at Julian day 310 in 2006, when ΔQ_t drops below -600 m^3 s^{-1}. This event may relate to large pontoons that sporadically cast anchor for several hours in the Berau River, disrupting the regular discharge distribution over the cross section.

[28] Figure 17 (top) displays the river discharge estimates $\hat{Q}_{1r}$ and $\hat{Q}_{2r}$, which range between 150 m^3 s^{-1} and 600 m^3 s^{-1} (omitting the minus sign). The difference between those estimates, denoted by ΔQ_r, has a maximum absolute value of 52 m^3 s^{-1}, and a standard deviation of 20 m^3 s^{-1}. Values of ΔQ_r are uncorrelated to the discharge magnitude and average out to 24 m^3 s^{-1}. The nonzero average indicates a small bias in either $\hat{Q}_{1r}$, $\hat{Q}_{2r}$, or in both. To remove this bias with the present methods, much more moving boat ADCP data are required, to obtain calibration information that

covers several oscillations of ΔQ_r. Figure 17 (bottom) displays the relative difference, which varies gradually over the measurement period.

[29] The variation in ΔQ_t and in ΔQ_r can be explained from intratidal and subtidal variation in f, respectively. Variation in f, in turn, can be attributed to the physical mechanisms governing the transverse exchange of momentum in the channel. The cross-river redistribution of momentum may depend on temporal variation in hydraulic roughness, due to the evolution of bed forms. Figure 11 shows that width-averaged values of z_0 feature constant periods during flood and ebb. This notwithstanding, intratidal variations in bed forms may alter local roughness values, steering the flow away from locations with a relatively high hydraulic roughness.

7. Discussion

[30] Crucial in the approach adopted herein is the determination of the effective roughness length (z_0), parameterizing river bed roughness, which was used to convert single point HADCP data to specific discharge. In general, values of z_0 can be estimated (1) using predictive formulas based on scaling arguments, relating it to grain sizes and bed forms [*Yalin*, 1992; *Wilcock*, 1996], (2) fitting flow velocity or Reynolds stress estimates to theoretical profiles expected from the law of the wall [*Lueck and Lu*, 1997; *Cheng et al.*, 1999] or (3) assimilating water level and flow velocity data to an analytical or numerical model [*Spitz and Klinck*, 1998; *Li et al.*, 2004]. The second approach is most accurate, provided that data from a rigid deployment are available. For moving boat ADCP measurements, Doppler noise and turbulence components in a signal are not readily isolated from the contribution by flow velocity. This has led *Sime et al.* [2007] to conclude that when estimating bed shear stress from moving boat ADCP measurements, the use of a rough estimate of z_0 is preferred over directly fitting both z_0 and u_* to individual velocity profiles. The present study shows that both z_0 and u_* can be obtained from repeated ADCP transect
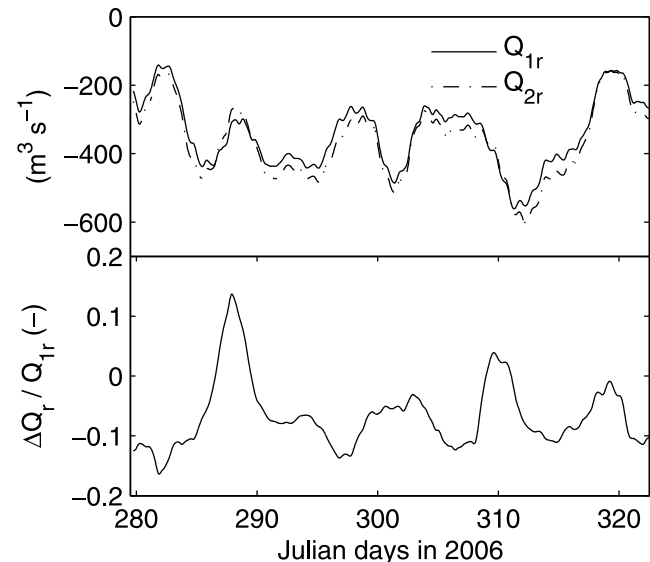

Figure 17. Variation of river discharge from $\hat{Q}_{1r}$ and $\hat{Q}_{2r}$, representing two mutually independent discharge estimates derived from HADCP measurements.

measurements, without prior knowledge about the bed composition, provided that a large number of ADCP transect measurements is available to filter out the contributions of noise and especially turbulence.

[31] *Nihei and Kimizu* [2008] introduced a new computational method to obtain river discharge estimates by assimilating HADCP data with a numerical model. The fundamental equation in their model represents a simplified momentum balance, in which terms representing longitudinal advection, diffusion and temporal acceleration are replaced by a single term. This term is treated as a vertically uniform calibration parameter in the assimilation procedure. Indeed, assimilating HADCP data with a numerical model may yield potentially improved results. However, the vertical two-dimensional, steady state approach adopted by *Nihei and Kimizu* [2008] will be inappropriate in the tidal river bend in the present study. The crucial aspects that would have to be resolved in the model concern the horizontal exchange of momentum, whereas the vertical flow structure can be modeled by the law of the wall. This calls for a horizontal two-dimensional modeling approach, and the use of a turbulence closure scheme capable of capturing the transverse momentum exchanges that are supposedly caused by bed roughness variation, acting on the secondary flow induced by flow curvature [e.g., *Blanckaert and De Vriend*, 2003]. If indeed bed form dynamics has an appreciable control over the cross-river discharge distribution, as argued in section 6, then assimilating data to a hydraulic model will not improve the conversion of HADCP data to discharge substantially unless the morphodynamics of the bed is resolved.

[32] Key features in the morphology of the bed as observed in Figure 2 are the dunes with a wavelength (λ) of roughly 25 m, and a height (Δ) in the order of 1 m. Considering that the dunes are at an angle of about 45 degrees relative to the flow, the dune length in the flow direction is about 35 m. Using the values of D_{50} and D_{90} inferred from the bed samples taken in the dune field, and representative values of z_0, h and u, an estimation can be made of the values of λ and Δ that can be expected in case of a unidirectional river flow. According to *Van Rijn* [1984], $\lambda = 7.3h$, which yields $\lambda = 51$ m at a depth of 7 m. Attributing $h = 7$ m and $z_0 = 10^{-2}$ m (corresponding to ebb flow), then the formulas provided by *Vanoni and Brooks* [1957] and *Van Rijn* [1984] predict that the threshold of sediment motion occurs at 0.35 m s^{-1}, and Δ peaks at a constant velocity of 0.85 m s^{-1}, when $\Delta = 0.78$ m. The latter prediction is lower than the observed value, suggesting that the bidirectional flow in the Berau River results in comparatively steeply sloped bed forms that are higher than what is attainable under unidirectional flow conditions. The oblique orientation of the bed forms at the measurement location further indicates that the mechanisms causing the genesis of bed forms in tidal river bends are fundamentally different from what is generally observed in rivers.

[33] The values of z_0 inferred from boat-mounted ADCP measurements in the dune field, shown in Figure 12, can be compared with the predictions from the theory of dunes. On the basis of an extensive data set, *Van Rijn* [1984] obtained:

$$k_b = 3D_{90} + 1.1\Delta\left(1 - e^{25\Delta/\lambda}\right) \qquad (22)$$

Attributing $\Delta = 1$ m, $\lambda = 35$ m and $D_{90} = 798$ μm, k_b is estimated to equal 0.83 m, and $z_0 = k_b/30 = 1.88 \; 10^{-2}$ m. This matches well with the observed values of z_0 during ebb flow.

8. Conclusions

[34] A semideterministic, semistochastic method was developed to convert HADCP velocity measurements into estimates of discharge in a 400 m wide section of the River Berau. The deterministic part relies on the validity of the law of the wall, to calculate specific discharge from single depth HADCP velocity data and a local estimate of the hydraulic roughness length z_0. Values of z_0 across the river transect were inferred from boat-mounted ADCP data covering a tidal cycle, that were filtered to remove the influences of turbulence and Doppler noise. Transverse profiles of z_0 were obtained during ebb and flood, showing a high consistency especially during the ebb period. Local values of z_0 were assumed to be constant for periods of ebb and flood, which allowed to convert HADCP data to range-dependent specific discharge estimates, without additional boat measurements. Specific discharge varies out of phase with total discharge in tidal rivers, as a result of inertial effects. In the River Berau, the specific discharge variation near the shores leads the discharge variation in the central part by about fifteen minutes. The specific discharge is therefore regressed against time-shifted total discharge, which constitutes the stochastic part of the method. On the basis of this regression, estimates of discharge can be obtained from specific discharge at any location along the HADCP measuring range.

[35] Corresponding mean velocity estimates from low-pass filtered HADCP data and boat-mounted ADCP data were compared. In a midfield range between 50 m and 120 m from the shore, measurements from the HADCP agreed well with the boat-mounted ADCP measurements. In this range, the slopes of regression lines through corresponding mean velocity estimates ranged between 0.96 and 1.04. Root-mean-square differences between those estimates were around 0.04 m s^{-1}, showing no dependency on the distance to the HADCP transducers. In the near-field range up to 50 m from the shore, HADCP derived velocity estimates were biased high, when compared with the corresponding boat-mounted ADCP estimates. It was argued that the HADCP measurements may outperform boat-mounted ADCP measurements, which were taken under sharp turning of the boat, resulting in error introduced by tilting of the boat. In the far-field range between 120 and 150 m, the HADCP estimates of mean velocity were biased low, which was attributed to sidelobe effects, corrupting the HADCP data in that range.

[36] Three weeks of HADCP velocity measurements in the midfield range were converted to an array of mutually independent time series of total discharge. The midfield range was divided in two parts of equal length. Discharge estimates were averaged over each part, yielding two time series of total discharge that were compared to investigate the internal consistency of the HADCP discharge estimates. The total discharge was decomposed in a tidal component and a subtidal component that primarily represents river discharge, and these were analyzed separately. The tidal discharges ranged between 2500 m^3 s^{-1} during flood and -2000 m^3 s^{-1} during ebb. The difference between estimates of tidal discharge from the two parts had a standard
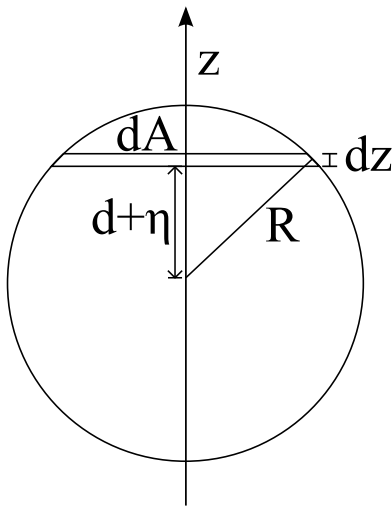
Figure A1. Cross section of an acoustic beam, intersecting with the water surface at $z = \eta$. Intersection of an acoustic beam with the water surface lowers the centroid of the ensonified water volume.

deviation of 93 m^3 s^{-1}, and its absolute value remained below 200 m^3 s^{-1} for 97% of time. River discharges ranged between 150 m^3 s^{-1} and 600 m^3 s^{-1} during the measurements. The difference between the river discharge estimates from the two parts had a standard deviation of 20 m^3 s^{-1}, and had a maximum absolute value of 52 m^3 s^{-1}. The differences in discharge estimates from the two parts were attributed to mechanisms of transverse exchange of momentum, enhancing temporal variation in the discharge distribution over the cross section.

Appendix A

[37] Considering a circular cross section of an acoustic beam with radius r, intersecting the water surface, the level difference between the centroid of the ensonified water area and the central beam axis can be calculated according to

$$\Delta z = \frac{\int z' dA}{\int dA} \quad (A1)$$

where $z' = z + d$ is a vertical coordinate pointing upward with the origin at the central beam axis, A is the ensonified water area and the infinitesimally small area dA is given by (Figure A1)

$$dA = 2\left(r^2 - z'^2\right)^{\frac{1}{2}} dz' \quad (A2)$$

Substituting this in equation (A1) and including integration limits yields

$$\Delta z = \frac{\int_{-r}^{d+\eta} z' \sqrt{r^2 - z'^2}\, dz}{\int_{-r}^{d+\eta} \sqrt{r^2 - z'^2}\, dz'} \quad (A3)$$

which can be elaborated to obtain

$$\Delta z = \frac{\frac{2}{3}\left(r^2 - (d+\eta)^2\right)^{1.5}}{r^2 \sin^{-1}\frac{d+\eta}{r} + (d+\eta)\sqrt{r^2 - (d+\eta)^2} + \frac{1}{2}\pi r^2} \quad (A4)$$

References

Biron, P. M., S. N. Lane, A. G. Roy, K. F. Bradbrook, and K. S. Richards (1998), Sensitivity of bed shear stress estimated from vertical velocity profiles: The problem of sampling resolution, *Earth Surf. Processes Landforms*, 23, 133–139.

Blanckaert, K., and H. J. de Vriend (2003), Nonlinear modeling of mean flow redistribution in curved open channels, *Water Resour. Res.*, 39(12), 1375, doi:10.1029/2003WR002068.

Boiten, W. (2008), *Hydrometry—A Comprehensive Introduction to the Measurement of Flow in Open Channels*, 247 pp., CRC Press, Boca Raton, Fla.

Chen, Y.-C., and C.-L. Chiu (2002), An efficient method of discharge measurement in tidal streams, *J. Hydrol.*, 265, 212–224.

Chen, Y.-C., and C.-L. Chiu (2004), A fast method of flood discharge estimation, *Hydrol. Processes*, 18, 1671–1684.

Cheng, R. T., C.-H. Ling, and J. W. Gartner (1999), Estimates of bottom roughness length and bottom shear stress in South San Francisco Bay, California, *J. Geophys. Res.*, 104, 7715–7728.

Chiu, C.-L., and S.-M. Hsu (2006), Probabilistic approach to modeling of velocity distributions in fluid flows, *J. Hydrol.*, 316, 28–42.

Chiu, C.-L., and N. C. Tung (2002), Maximum velocity and regularities in open-channel flow, *J. Hydraul. Eng.*, 128, 390–398.

Dinehart, R. L., and J. R. Burau (2005), Repeated surveys by acoustic Doppler current profiler for flow and sediment dynamics in a tidal river, *J. Hydrol.*, 314, 1–21.

Dingman, S. L. (2007), Comment on "Probabilistic approach to modeling of velocity distributions in fluid flows" by C.-L. Chiu and S.-M. Hsu, Journal of Hydrology 316:28–42, *J. Hydrol.*, 335, 419–428.

Hauet, A., A. Kruger, W. Krajewski, A. Bradley, M. Muste, J. D. Creutin, and M. Wilson (2008), Experimental system for real-time discharge estimation using an image-based method, *J. Hydraul. Eng.*, 13, 105–110.

Henderson, F. M. (1966), *Open Channel Flow*, 544 pp., Macmillan, New York.

Hoitink, A. J. F., and P. Hoekstra (2005), Observations of suspended sediment from ADCP and OBS measurements in a mud-dominated environment, *Coastal Eng.*, 52, 103–118.

Ikeda, S., M. Yamasaka, and J. F. Kennedy (1990), 3-dimensional fully-developed shallow-water flow in mildly curved bends, *Fluid Dyn. Res.*, 6, 155–173.

Le Blond, P. (1979), Forced fortnightly tides in shallow rivers, *Atmos. Ocean*, 17, 253–264.

Le Coz, J., G. Pierrefeu, and A. Paquier (2008), Evaluation of river discharges monitored by a fixed side-looking Doppler profiler, *Water Resour. Res.*, 44, W00D09, doi:10.1029/2008WR006967.

Li, C., A. Valle-Levinson, L. P. Atkinson, K. C. Wong, and K. M. M. Lwiza (2004), Estimation of drag coefficient in James River Estuary using tidal velocity data from a vessel-towed ADCP, *J. Geophys. Res.*, 109, C03034, doi:10.1029/2003JC001991.

Lueck, R. G., and Y. Y. Lu (1997), The logarithmic layer in a tidal channel, *Cont. Shelf Res.*, 17, 1785–1801.

Marmorino, G. O., C. L. Trump, and Z. R. Hallock (1999), Near-surface current measurements using a ship-deployed 'horizontal' ADCP, *J. Atmos. Oceanic Technol.*, 16, 1456–1463.

Muste, M., I. Fujita, and A. Hauet (2008), Large-scale particle image velocimetry for measurements in riverine environments, *Water Resour. Res.*, 44, W00D19, doi:10.1029/2008WR006950.

Nihei, Y., and A. Kimizu (2008), A new monitoring system for river discharge with horizontal acoustic Doppler current profiler measurements and river flow simulation, *Water Resour. Res.*, 44, W00D20, doi:10.1029/2008WR006970.

Perumal, M., T. Moramarco, B. Sahoo, and S. Barbetta (2007), A methodology for discharge estimation and rating curve development at ungauged river sites, *Water Resour. Res.*, 43, W02412, doi:10.1029/2005WR004609.

Pope, S. B. (2000), *Turbulent Flows*, 771 pp., Cambridge Univ. Press, Cambridge, U. K.

Schlax, M. G., and D. B. Chelton (1992), Frequency domain diagnostics for linear smoothers, *J. Am. Stat. Assoc.*, 87, 1070–1081.

Sime, L. C., R. I. Ferguson, and M. Church (2007), Estimating shear stress from moving boat acoustic Doppler velocity measurements in a large gravel bed river, *Water Resour. Res.*, 43, W03418, doi:10.1029/2006WR005069.

Soulsby, R. L., and K. R. Dyer (1981), The form of the near-bed velocity profile in a tidally accelerating flow, *J. Geophys. Res.*, 86, 8067–8074.

Spitz, Y. H., and J. M. Klinck (1998), Estimates of bottom and surface stress during a spring-neap cycle by dynamical assimilation of tide gauge observations in the Chesapeake Bay, *J. Geophys. Res.*, 103, 5531–5549.

Van Rijn, L. C. (1984), Sediment transport, part III: Bed forms and alluvial roughness, *J. Hydraul. Eng.*, 110, 1733–1754.

Vanoni, V. A., and N. H. Brooks (1957), Laboratory studies of the roughness and suspended load of alluvial streams, *Tech. Rep. E-68*, Sediment. Lab., Calif. Inst. of Technol., Pasadena.

Wilcock, P. R. (1996), Estimating local shear stress from velocity observations, *Water Resour. Res.*, 32, 3361–3366.

Xu, J. P., and L. D. Wright (1995), Tests of bed roughness models using field data from the Middle Atlantic Bight, *Cont. Shelf Res.*, 15, 1409–1434.

Yalin, M. S. (1992), *River Mechanics*, 220 pp., Pergamon, Oxford, U. K.

————————————

A. J. F. Hoitink and B. Vermeulen, Hydrology and Quantitative Water Management Group, Wageningen University, NL-6700 AA Wageningen, Netherlands. (ton.hoitink@wur.nl)

F. A. Buschman, Institute for Marine and Atmospheric Research Utrecht, Department of Physical Geography, Utrecht University, NL-3508 TC Utrecht, Netherlands.